ACS NANO

www.acsnano.org

ARTICLE

Room Temperature Commensurate Charge Density Wave on Epitaxially Grown Bilayer 2H-Tantalum Sulfide on Hexagonal Boron Nitride

Wei Fu,[#] Jingsi Qiao,[#] Xiaoxu Zhao,[#] Yu Chen, Deyi Fu, Wei Yu, Kai Leng, Peng Song, Zhi Chen, Ting Yu, Stephen J. Pennycook, Su Ying Quek,[*] and Kian Ping Loh[*]

Cite This: *ACS Nano* 2020, 14, 3917−3926

Read Online

ACCESS | Metrics & More | Article Recommendations | Supporting Information

ABSTRACT: **The breaking of multiple symmetries by periodic lattice distortion at a commensurate charge density wave (CDW) state is expected to give rise to intriguing interesting properties. However, accessing the commensurate CDW state on bulk TaS_2 crystals typically requires cryogenic temperatures (77 K), which precludes practical applications. Here, we found that heteroepitaxial growth of a 2H-tantalum disulfide bilayer on a hexagonal-boron nitride (*h*-BN) substrate produces a robust commensurate CDW order at room temperature, characterized by a Moiré superlattice of 3 × 3 TaS_2 on a 4 × 4 *h*-BN unit cell. The CDW order is confirmed by scanning transmission electron microscopy and Raman measurements. Theoretical calculations reveal that the stabilizing energy for the CDW phase of the monolayer and bilayer 2H-TaS_2-on-*h*-BN substrates arises primarily from interfacial electrostatic interactions and, to a lesser extent, interfacial strain. Our work shows that engineering interfacial electrostatic interactions in an ultrathin van der Waals heterostructure constitutes an effective way to enhance CDW order in two-dimensional materials.**

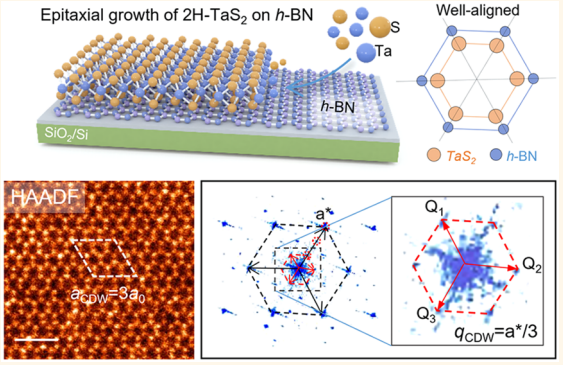

KEYWORDS: *charge density wave, two-dimensional transition metal dichalcogenides, molecular beam epitaxy, interfacial electrostatic interaction, Moiré superlattice*

A charge density wave (CDW) state is a macroscopic quantum state showing strong coupling between periodic lattice distortion and electron density modulation.[1−4] The CDW state engenders spontaneously broken symmetries, leading to novel phenomena.[5−9] For example, the CDW in 1T-TiS_2 breaks inversion symmetry with an axial vector resulting in a chiral state.[8] Phase transitions between different CDW states can be electrically switched, and the abrupt change of resistance and hysteresis during such phase transitions can be used for building logic gates and circuits without the need for field effect transistors.[10,11] However, practical applications of CDW-based devices are hampered by the fact that CDW ordering is usually accessed only at cryogenic temperatures.[12,13] The CDW transition temperature, T_{CDW}, between the normal and the CDW phase occurs at 33 K for $NbSe_2$[14] and at 78 K for 2H-TaS_2 bulk crystals,[15,16] greatly limiting their practical applications. Hence, there is a search for materials that exhibit room-temperature commensurate CDWs. Theoretical studies have focused on the impact of strain and charge doping on the soft phonon mode that stabilizes the CDW transition of monolayer or bulk metallic transition metal dichalcogenides (TMDs).[17,18] For example, it has been shown that tensile strain can stabilize the CDW phase in 1T-$TiSe_2$[17] and 1T-TaS_2,[19] and charge doping can suppress the CDW phase in 1T-$TiSe_2$,[17] 1H-TaS_2,[19] and 2H-$NbSe_2$.[20] Strategies such as reducing the thickness have also been applied in an attempt to enhance T_{CDW}.[3,21]

Herein, we discover that when atomically thin hexagonal TaS_2 is epitaxially grown on hexagonal-boron nitride (*h*-BN), a room temperature 3 × 3 commensurate CDW state is stabilized, as revealed by STEM and Raman measurements. The T_{CDW} is increased from 78 K for bulk 2H-TaS_2 to higher than room temperature for bilayer TaS_2 grown epitaxially on *h*-BN. The room temperature CDW phase cannot be observed in epitaxially grown TaS_2/graphene or physically transferred

Received: January 11, 2020
Accepted: February 12, 2020
Published: February 12, 2020

https://dx.doi.org/10.1021/acsnano.0c00303
ACS Nano 2020, 14, 3917−3926

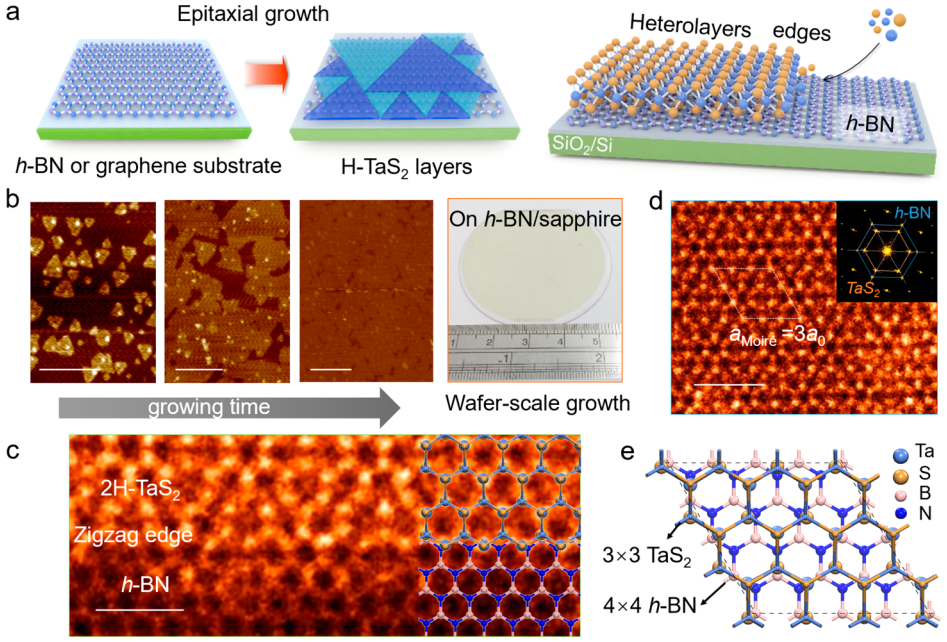

Figure 1. Epitaxial growth of atomic 2H-TaS_2 layers. (a) Schematic representation of the MBE growth of a high-quality 2H-TaS_2 film. The blue and green triangles denote the 0° and 60°-rotated domains, respectively. (b) AFM images showing the growth of TaS_2 crystals as a function of time and optical image of as-grown 2H-TaS_2/*h*-BN/sapphire heterolayers on 2-in. wafers. (c) STEM-measured zigzag edge of a TaS_2 flake on *h*-BN. Scale bar is 1 nm. (d) HAADF-STEM image of bilayer 2H-TaS_2/*h*-BN heterolayers. $a_{Moiré}$ and a_0 represent the in-plane lattice constants of a Moiré heterolayers and 1 × 1 H-TaS_2 unit cell, respectively. The insert is the corresponding fast Fourier transform. Scale bar is 1 nm. (e) Schematic of the epitaxially matched heterolayers unit cell corresponding to panel (d).

TaS_2/*h*-BN (rotationally misoriented).[22] Density functional theory (DFT) calculations show that the stabilization of the CDW phase arises mainly from interfacial electrostatic interaction between TaS_2 and *h*-BN in the Moiré superlattice of 3 × 3 TaS_2 on 4 × 4 *h*-BN, with negligible charge transfer between TaS_2 and *h*-BN. In contrast, there is a large charge transfer from graphene to TaS_2, which suppresses the CDW phase.[22] Our work indicates that the CDW phase transition temperatures of atomically thin metallic TMDs can be enhanced significantly by growing the CDW host epitaxially on *h*-BN, on which the Moiré electrostatic modulation plays an important role in stabilizing the CDW order.

RESULTS AND DISCUSSION

Molecular Beam Epitaxy Growth of Wafer-Scale, Bilayer TaS_2 on *h*-BN. Using molecular beam epitaxy (MBE), bilayer TaS_2 crystals were epitaxially grown on an *h*-BN or graphite crystal. Ultrapure tantalum and sulfur molecular beams were evaporated by an e-beam evaporator and a valved sulfur cracker cell, respectively. Due to the hexagonal symmetry of the crystal, as-grown TaS_2 domains show two types of orientations (0° and rotated by 60°) on the *h*-BN or graphite substrate (as depicted in Figure 1a). With longer growth time, the domains merge to form a continuous film (Figure 1b). Compared with the theoretical monolayer thickness (~0.66 nm) of TaS_2, the film thickness of ~1.18 nm as measured by the height profiles of atomic force microscope (AFM) images in Figure S1 indicate that the TaS_2 forms bilayers on *h*-BN. On a large *h*-BN/sapphire wafer, a wafer-scale atomic TaS_2/*h*-BN hybrid film was successfully grown (Figure 1b), and the film characterizations are shown in Figure S2. The growth follows the Frank−van der Merwe growth mode as revealed by AFM images of the nuclei and partially coalesced film in Figure 1b. Aberration corrected scanning transmission electron microscopy−high angle annular dark field (STEM-HAADF) images of a step edge in Figure 1c show epitaxial growth along the Ta−Ta/S−S zigzag direction.[23−25]

The STEM-HAADF image of the heterolayers in Figure 1d shows a honeycomb lattice that is characteristic of the H-phase polymorph, in which the sulfur atoms are arranged in a trigonal prismatic arrangement around the Ta atoms. Raman measurements (Figure 3) and XPS spectra (Figure S3) also evidence that the as-grown film is H-phase TaS_2. TaS_2 grown on *h*-BN reveals a signature honeycomb structure as imaged by STEM-HAADF, which is indicative of an AA′-stacked bilayer (Figure 1e). The corresponding fast Fourier transform (FFT) diffraction pattern inserted in Figure 1d demonstrates that the bilayer 2H-TaS_2 diffraction spots are aligned with respect to the crystallographic orientation of the underlying *h*-BN crystal, revealing that the TaS_2 layer grows epitaxially on the *h*-BN. Additionally, a well-defined Moiré pattern is observed on the TaS_2/*h*-BN heterolayers with a periodicity of ~10 Å (Figure 1d,e). The Moiré superlattice is constructed by a 3 × 3 TaS_2 on 4 × 4 *h*-BN. This superlattice is consistent with the excellent lattice match between 3 × 3 TaS_2 and 4 × 4 *h*-BN, with TaS_2 experiencing a tensile strain of only ~0.9% (Table S1).

Scanning Transmission Electron Microscopic Study of Room-Temperature Commensurate CDW Ordering. Medium angle ADF (MAADF) imaging collects a high fraction of coherently elastic scattered electrons in which the image contrast is sensitive to small atomic displacements.[26,27] Hence, MAADF imaging was used to probe the existence of periodic intensity changes due to the room-temperature CDW ordering in the bilayer 2H-TaS_2 on *h*-BN. In this case, the TaS_2 bilayer was directly grown by MBE on an *h*-BN (or few-layer graphene) flake that was pretransferred onto a TEM grid to avoid sample degradation caused by solution-based transfer

https://dx.doi.org/10.1021/acsnano.0c00303
ACS Nano 2020, 14, 3917−3926

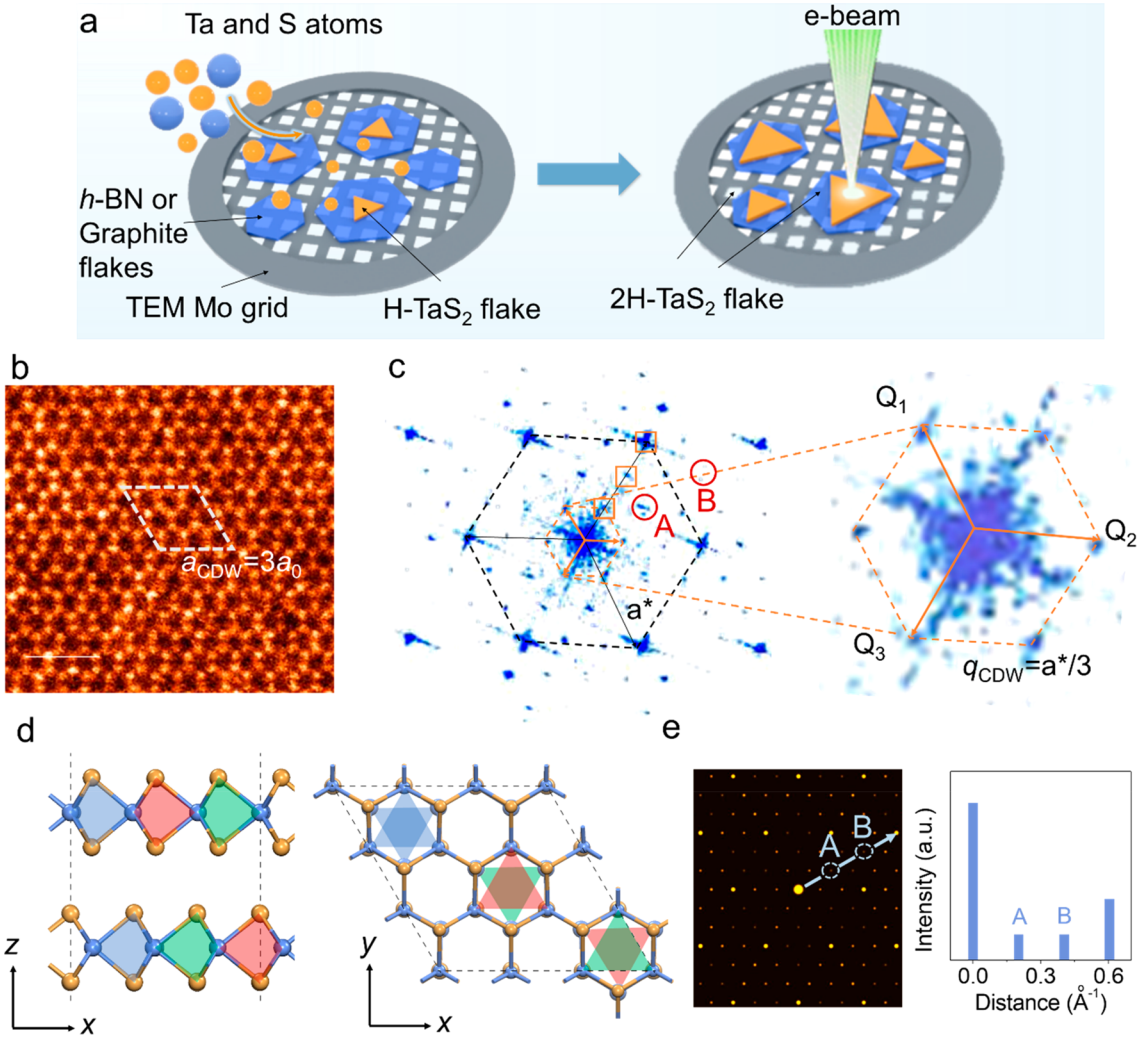

Figure 2. STEM study of room-temperature commensurate CDW. (a) Schematic showing direct MBE growth of TaS_2 on BN flakes transferred onto a Mo grid and subsequent STEM analysis. (b) Medium-angle annular dark-field (MAADF) STEM image of bilayer 2H-TaS_2/*h*-BN hybrid and (c) Fourier transform of the atomically resolved MAADF image in b, showing atomic (black) and CDW (orange) reciprocal cells. a^* is the reciprocal atomic vector, and q_i (i = 1,2,3) are the CDW ones. Magnified view of the CDW cell (orange) in (c). $q_{CDW} = a^*/3$, revealing the presence of 3 × 3 periodicity due to the CDW. (d) Side (left) and top (right) view of the atomic structure of AA′-bilayer 3 × 3 trihollow CDW H-TaS_2. Blue, green, and pink triangles are used to group Ta atoms. The Ta−Ta distances decrease by 3.7% and 1.7% in the blue and green triangles, respectively, while the Ta−Ta distances in the pink triangle increase by 2.9%. (e) Simulated FFT image and the schematic intensity line profile (not drawn to scale) along the blue arrow in the upper panel of bilayer trihollow CDW H-TaS_2.

methods (Figure 2a). The trigonal prismatic structure of the 2H phase is clearly observed in the STEM-MAADF image in Figure 2b. The superlattice spots in the FFT diffraction pattern (orange squares in Figure 2c) indicate the existence of a 3 × 3 TaS_2 superlattice. The q_{CDW} vectors calculated in Figure 2c are well aligned with atomic vectors of prismatic TaS_2 and correspond to a commensurate 3 × 3 CDW state. The 3 × 3 superlattice is consistent with the 3 × 3 periodic CDW order reported in the 2H-TaS_2 bulk crystal at 78 K,[14] which arises from large electron−phonon coupling in TaS_2.[28]

To identify if the *h*-BN substrate plays a special role in enhancing CDW order in epitaxially grown 2H-TaS_2/*h*-BN, we also examined if the chemical exfoliated bilayer H-TaS_2 and epitaxially grown bilayer H-TaS_2 on graphene shows similar 3 × 3 periodicity. On an exfoliated, freestanding bilayer TaS_2 flake (schematic shown in Figure 3a), the signature honeycomb structure of 2H-TaS_2 is seen in the MAADF-STEM image in Figure 3b. From the corresponding FFT diffraction pattern in Figure 3c, only the 1 × 1 diffraction spots of 2H-TaS_2 are seen. This indicates that the room temperature CDW state observed on bilayer 2H-TaS_2/*h*-BN is not intrinsic to bilayer 2H-TaS_2 crystals. Moreover, on the MBE grown bilayer H-TaS_2 /monolayer graphene sample (depicted in Figure 3d), two types of domain orientations (0° and rotated by 60°) are observed in Figure 3e, similar to the sample grown on *h*-BN. High-quality atomic honeycomb structure is also observed in the MAADF-STEM image in Figure 3f. However, the inset FFT pattern only displays normal 1 × 1 2H-TaS_2 diffraction spots, and no CDW superlattice is detected. We can conclude that epitaxial growth alone is insufficient to guarantee the 3 × 3 CDW phase, despite the fact that graphene and *h*-BN share very similar lattice constants (Table S1).

Closely examining the 3 × 3 CDW atomic structure in our MBE grown bilayer H-TaS_2/*h*-BN sample reveals that besides the diffraction spots corresponding to the 3 × 3 real space lattice (Figure 2c), the Fourier transform of the STEM-

https://dx.doi.org/10.1021/acsnano.0c00303
ACS Nano 2020, 14, 3917−3926

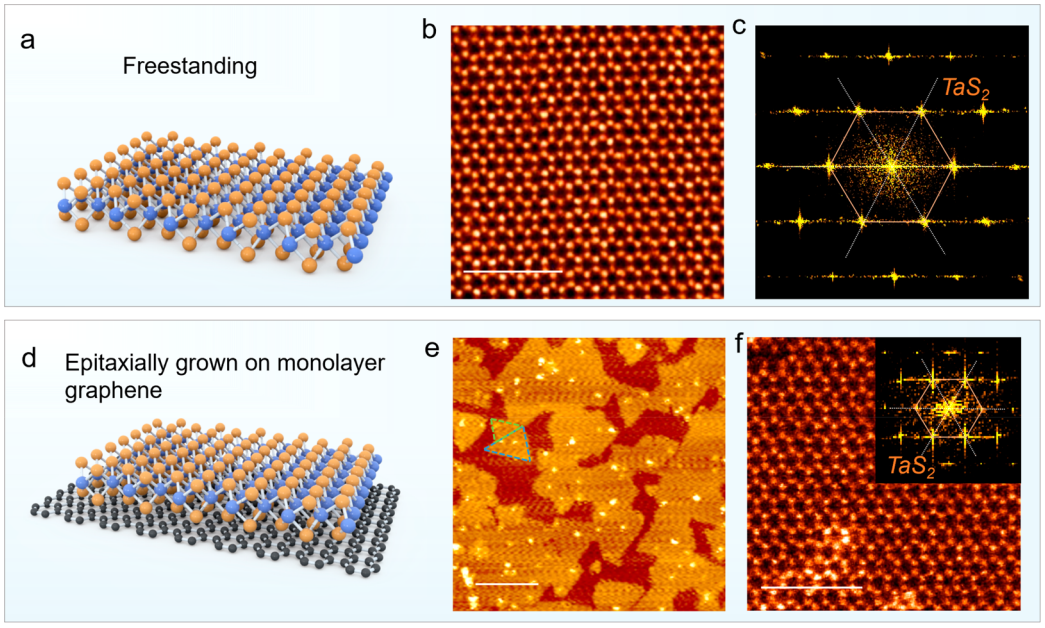

Figure 3. STEM study of freestanding 2H-TaS_2 and epitaxially grown 2H-TaS_2/graphene. (a) Schematic of freestanding 2H-TaS_2. (b) MAADF STEM image of freestanding 2H-TaS_2. (c) The inset is the corresponding Fourier transform. (d) Schematic of 2H-TaS_2 epitaxially grown on graphene. (e) AFM image of 2H-TaS_2 epitaxially grown on monolayer graphene. (f) MAADF STEM image of epitaxially grown 2H-TaS_2/graphene and the corresponding Fourier transform, showing a 1 × 1 pristine 2H-TaS_2 lattice structure on the graphene monolayer.

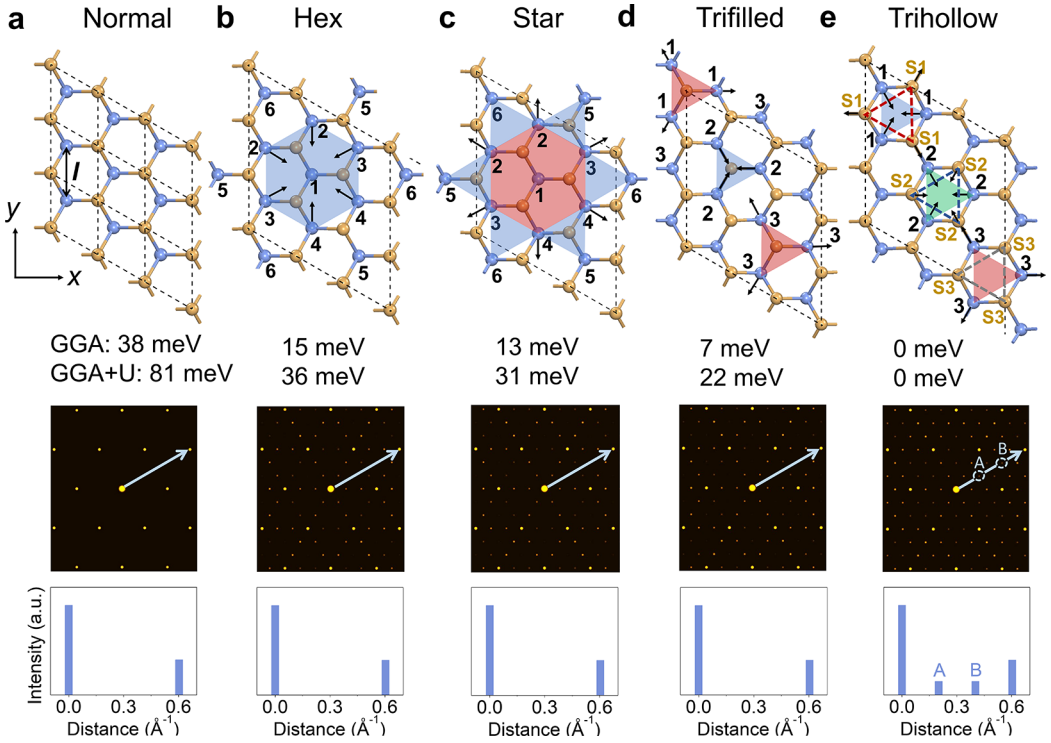

Figure 4. Geometric structures, simulated FFT image, and the schematic intensity line profile of monolayer normal (a), hex-CDW (b), star-CDW (c), trifilled-CDW (d), and trihollow-CDW (e) H-TaS_2. Arrows show the directions of motion of Ta atoms compared to the normal phase. FFT simulation images and intensity line profiles of the blue line for these structures are shown below for each configuration. Among the common CDW structures, only trihollow-CDW shows A and B dots along the blue arrows in the FFT images. The intensity line profiles and the lengths of the arrows are not drawn to scale. For the trihollow-CDW structure in (e), blue, green, and pink triangles are used to group Ta atoms. The Ta−Ta distances decrease by 3.8% and 2.0% in the blue and green triangles, respectively, while the Ta−Ta distances in the pink triangle increase by 3.0%. The S atoms in the trihollow-CDW structure are also labeled S1−S3. The S1 atoms move away from one another, and the S2 atoms move toward each other. The distances between S3 atoms remain the same.

MAADF image shows additional diffraction spots, labeled as A and B (red circles) in Figure 2c. We performed DFT calculations using the generalized gradient approximation (GGA) together with nonlocal van der Waals (vdW)

https://dx.doi.org/10.1021/acsnano.0c00303
ACS Nano 2020, 14, 3917−3926

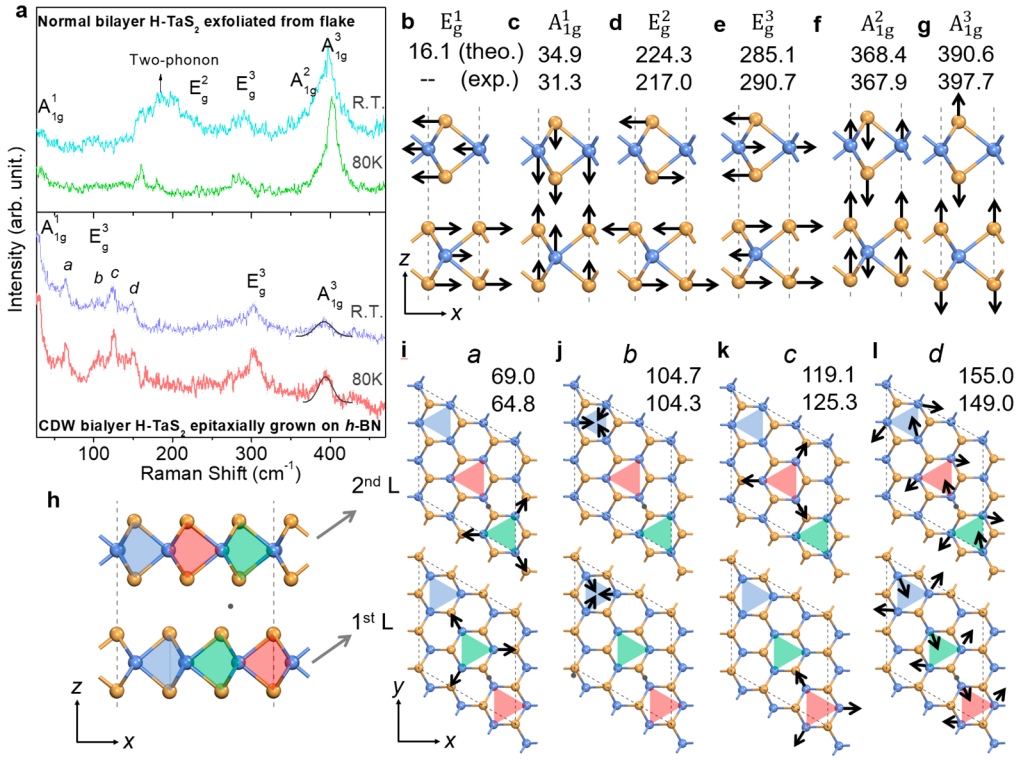

Figure 5. Raman studies of room temperature commensurate CDW ordering in bilayer H-TaS_2 epitaxially grown on *h*-BN. (a) Raman spectra of bilayer TaS_2 exfoliated flake and epitaxially grown bilayer TaS_2-on-*h*-BN at room temperature and 80 K. Vibrational modes are labeled. (b–g) Vibrational frequencies and displacements of all Raman active modes in bilayer TaS_2. (h) Side view of the most stable CDW bilayer TaS_2. The gray dot shows the inversion symmetry center. (i–l) Vibrational frequencies and displacements of modes *a–d* labeled in (a) in CDW bilayer TaS_2. Therein, the vibrational modes of the first and second layers in CDW bilayer TaS_2 are separately presented. All frequencies are given in wavenumbers (cm^{-1}). Arrows indicate the vibrational displacements of the modes. Blue, green, and pink triangles are used to group Ta atoms according to their relative displacements.

correlation for the exchange-correlation functional (optB86b-vdW[30,31]). Our DFT calculations show that out of the four 3 × 3 CDW atomic structures (Figure 4) commonly considered in the literature, only the trihollow CDW structure produces these A and B spots in the simulated diffraction pattern of the monolayer (Figure 4e) and AA′ stacked bilayer (Figure 2d,e). These results provide clear evidence that the 3 × 3 CDW phase in H-TaS_2 adopts the trihollow CDW structures (Figure 4e,d), which is also consistent with the CDW structure reported for H-$NbSe_2$.[29] Indeed, our DFT GGA calculations for monolayer H-TaS_2 show that the trihollow structures (Figure 4e) are 7 meV, 13 meV, 15 meV, and 38 meV more stable than those of the trifilled-CDW (Figure 4d),[29] star-CDW (Figure 4c),[32] hex-CDW (Figure 4b),[33] and 3 × 3 normal phase H-TaS_2 (Figure 4a), respectively. The energy differences among different phases were also calculated by the GGA+*U* (DFT+*U*) method (Figure 4), where a Hubbard *U* term is added to the DFT Hamiltonian to take into account strong on-site Coulomb interactions of localized Ta *d* electrons.[34] *U* = 2.5 eV was estimated using a linear-response method.[35] Details of all these CDW structures are provided in Table S2. The trihollow-CDW structure of interest here is characterized by triangular groups of Ta and S atoms, as shown in Figure 4e. Atoms in the same group move away from one another, move toward one another, or do not move relative to one another (see Figure 4e caption and Table S2).

We compute the phonon spectra of bilayer normal phase H-TaS_2 (Figure S5a) and find that a soft phonon mode with large imaginary frequency is obtained at $\boldsymbol{q}$ = [0.33, 0, 0], consistent with the formation of a 3 × 3 CDW phase in bilayer H-TaS_2. The most stable CDW phase (Figure 2d) in the AA′-bilayer H-TaS_2 system was identified by considering different relative stacking orientations of two monolayers in the trihollow structure (Figure S4).

Raman Study of Phonon Vibration Modes in Room-Temperature CDW Ordering. The CDW phase is accompanied by the emergence of optically active Raman modes, thus Raman spectroscopy is widely used to charactize the vibrational properties of the CDW materials.[3] We first consider the vibrational properties of 2L AA′ H-TaS_2 in its normal phase ($P\bar{3}m1$ space group (No. 164)). The vibrational modes of even layer (*n* atoms) AA′ TaS_2 (normal phase) decompose into four types of irreducible representations at the Γ point: $\Gamma^{AA'\text{-}TaS_2}_{\text{even-L}} = \frac{n}{2}(A_{1g} \oplus A_{2u} \oplus E_g \oplus E_u)$. Therein, the A_{1g} (Figure 5c,f,g) and E_g (Figure 5b,d,e) modes are Raman active. A_{2u} (Figure S5b,f,g) and E_u (Figure S5c,d,e) modes are infrared active. Figure 5a shows the experimental Raman spectra of TaS_2 at room temperature and 80 K. It is clear that the Raman spectrum of the exfoliated flake is different from that of TaS_2 epitaxially grown on *h*-BN. For the exfoliated flake, all the Raman frequencies predicted for the normal phase TaS_2 are experimentally observed (see Figure 5b for frequencies) except for the shear mode located at low wavenumbers (E^1_g (16.1 cm^{-1})); the latter is beyond the detection limition of the equipment. A broad peak around 185 cm^{-1} in Figure 5a corresponds to a two-phonon mode, which is commonly observed in the normal phase of group-VB H-

https://dx.doi.org/10.1021/acsnano.0c00303
ACS Nano 2020, 14, 3917–3926

Table 1. CDW Formation Energies of TaS_2 and TaS_2/*h*-BN Heterostructures

	ΔE (meV)			
	monolayer (GGA)	bilayer (GGA)	monolayer (GGA+*U*)	bilayer (GGA+*U*)
TaS_2	−38	−66	−81	−145
TaS_2 (0.9% tensile strain corresponding to the Moire superlattice match with *h*-BN)	−42	−75	−85	−151
TaS_2/*h*-BN structure I [I′]	−57 [−5]	−86 [−41]	−102 [−52]	−168 [−119]
TaS_2/*h*-BN structure II [II′]	−61 [−9]	−91 [−43]	−108 [−54]	−174 [−122]

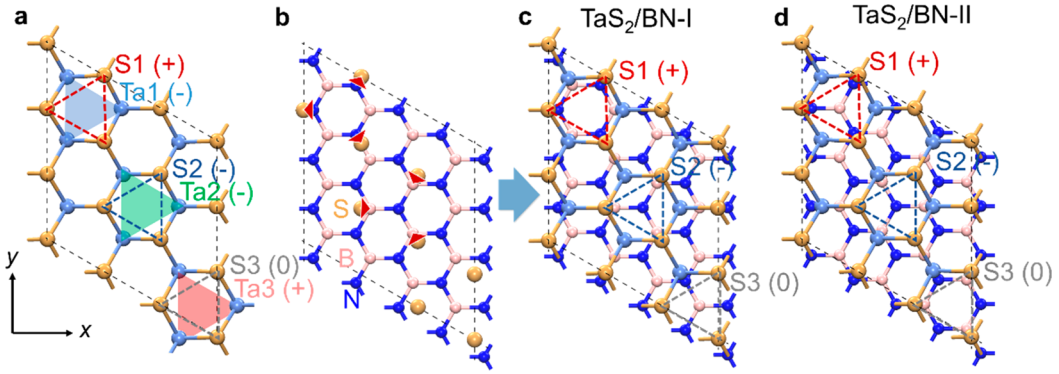

Figure 6. Effect of the *h*-BN substrate on the CDW phase. (a) Top view of the atomic structure of monolayer 3 × 3 CDW TaS_2, shown without the *h*-BN substrate. (b) *h*-BN substrate with S atoms overlaid in the TaS_2/*h*-BN commensurate superlattice. (c, d) Atomic structures of TaS_2/*h*-BN-I and TaS_2/*h*-BN-II, two of the commensurate heterostructures considered in this work. The signs, + , −, and 0, refer to the increase or decrease in Ta−Ta distances or S−S distances within each colored triangle, relative to the freestanding monolayer TaS_2 phase. The red, dark blue, and gray dashed triangles are used to denote the groups S1 (+), S2 (−), and S3 (0), respectively. The red arrowheads in (b) show the direction of the forces exerted by the negatively charged N atoms and positively charged B atoms on the adjacent (negatively charged) S atoms. (b) to (c) shows a schematic to illustrate how the *h*-BN substrate favors the CDW state in TaS_2.

TMDs.[36,37] No peaks are detected from 40 to 150 cm^{-1} in the exfoliated sample.

Bilayer AA′-stacked CDW TaS_2 belongs to the $P\bar{3}m1$ space group. The inversion centers of the bilayer CDW structures are labeled by black dots in Figure 5h,i−l. Seven Raman peaks are clearly observed in Figure 5a for bilayer TaS_2 epitaxially grown on *h*-BN, which is different from the Raman spectra of exfoliated TaS_2. Using first-principles calculations, we find that these Raman peaks can be assigned to Raman active modes in AA′-stacked CDW bilayer TaS_2, as labeled in Figure 5. The corresponding theoretical/experimental frequencies are given as follows: A_{1g}^1 (31.9/28.9 cm^{-1}; Figure S6a), mode a (69.0/64.8 cm^{-1}; Figure 5i), mode b (104.7/104.3 cm^{-1}; Figure 5j), mode c (119.1/125.3 cm^{-1}; Figure 5k), mode d (155.0/149.0 cm^{-1}; Figure 5l), E_g^3 (301.2/301.7 cm^{-1} Figure S6e), and A_{1g}^3 (392.0/392.4 cm^{-1}; Figure S6f), respectively. In contrast to the Raman spectrum for exfoliated TaS_2, there is significant Raman intensity in the low frequency range of 40 to 150 cm^{-1} arising from CDW-related modes *a*−*d*. The Ta atoms in each supercell of the CDW phase can be distinguished into three groups (Figure 2d,e). We denote these three groups by green, blue, and pink triangles in Figure 5h−l. Modes *a*, *b*, and *c* (Figure 5i−k) involve predominantly the vibration of one of these groups of Ta atoms in each layer. The vibration of the Ta atoms in different groups leads to significant differences in frequency among these modes, consistent with the different Ta−Ta bond lengths in the different groups in the CDW structure. Mode *d* involves displacements of all the Ta atoms. Modes *a*−*d* are related to the E^1 (Figure S5h) and E^2/E^3 modes (Figure S5i,j) of the normal 2H phase bilayer TaS_2 at the K point (0.33, 0.33, 0), which folds to the Gamma point in the 3 × 3 CDW bilayer H-TaS_2 structure, enabling the phonon to be optically detected in the Raman spectra. The Raman peaks in the frequency range 40 to 150 cm^{-1} are strong signatures of the CDW phase. In addition, two-phonon modes detected in normal H-TaS_2 exfoliated from flakes disappear in bialyer H-TaS_2 epitaxially grown on *h*-BN, which is also an evidence to indicate the appearance of a CDW phase.[37,38] Thus, the Raman spectra in Figure 5a show that the CDW phase exists at between room temperature and 80 K for bilayer TaS_2 epitaxially grown on *h*-BN but not in exfoliated TaS_2.

Effect of the *h*-BN Substrate on the Stabilization of the CDW Phase in H-TaS_2. The very large increase in T_{CDW} for bilayer H-TaS_2 epitaxially grown on *h*-BN substrates (compared to both bulk and exfoliated bilayer H-TaS_2) indicates that the CDW phase of H-TaS_2 is remarkably stable on *h*-BN. We define the CDW formation energy per 3 × 3 TaS_2 unit cell to be $\Delta E = E_{CDW} - E_{Normal}$. ΔE values calculated by GGA and GGA+*U* methods show consistent results (Table 1). Here, we discuss the GGA results. In unstrained TaS_2 with no substrate, the ΔE values are −38 meV and −66 meV for monolayer and bilayer TaS_2, respectively (Table 1). Earlier theoretical studies have focused on the impact of strain on ΔE.[38,39] The *h*-BN substrate induces 0.9% tensile strain on TaS_2. Calculations show that this amount of strain increases the magnitude of ΔE by 4 and 9 meV for freestanding monolayer and bilayer TaS_2, respectively (Table 1). Significantly, when an *h*-BN substrate is included explicitly in the DFT calculations, taking TaS_2/*h*-BN structures I (II) as examples (I: Figure 6c; II: Figure 6d), ΔE becomes −57 (−61) meV for monolayer TaS_2 and −86 (−91) meV for bilayer TaS_2 (Table 1), which corresponds to a stabilization of the CDW phase by 19−23 meV and 20−25 meV, respectively. This clearly indicates that compared to interfacial stabilization by *h*-

https://dx.doi.org/10.1021/acsnano.0c00303
ACS Nano 2020, 14, 3917−3926

BN, strain alone accounts for only less than ~19% (monolayer) and ~45% (bilayer) of the change in ΔE. The maximum change in ΔE for strains up to 5% does not exceed 10 meV per layer (Figure S7), which indicates that the stabilization energy due to an interfacial effect by *h*-BN is larger than what can be achieved by strain alone for monolayer and bilayer TaS_2. We have considered a total of 18 different stacking orders for monolayer TaS_2 on *h*-BN (see Figure S8 for details), and we found that ΔE varies from ~−48 meV to −61 meV in all the geometry-optimized structures. These ΔE values indicate that the stabilization of the CDW phase is quite robust with respect to the specific stacking orientation. In all these heterostructures, the charge transfer between TaS_2 and *h*-BN is negligible. Structures I and II (Figure 6c,d, Table 1) are among the most stable of the heterostructures with different stacking orders.

In order to understand the nature of the interfacial interaction between TaS_2 and *h*-BN, and specifically to determine what causes the stabilization of the CDW phase, we create artificial structures I′ and II′, where the B and N atoms are swapped without allowing the positions of the atoms to relax. ΔE becomes −3 meV and −9 meV in structures I′ and II′, respectively (Table 1), much smaller than ΔE in isolated unstrained monolayer TaS_2. This indicates that, in these artificial structures, the CDW phase becomes strongly suppressed by the *h*-BN substrate. Importantly, this reveals that the positions of the B and N atoms relative to the S atoms play an important role in the interfacial stabilization mechanism in TaS_2. As shown in Figure 4, the trihollow-CDW structure is characterized by triangular groups of Ta and S atoms. Figure 6a,b illustrates these groups in greater detail. There are three groups of S atoms (Figure 6a). In group S1 (red dashed triangle), the S−S distances increase relative to the normal phase (S1: + indicating an increase in S−S distances); in group S2 (dark blue dashed triangle), the S−S distances decrease (S2: − indicating a decrease in S−S distances); and in group S3 (gray dashed triangle), the S−S distances remain the same (details in Table S2). These groups, S1, S2, and S3, are closely related to the corresponding three groups of the Ta atoms, denoted by blue, green, and pink triangles, respectively (Figure 6a). By examining the details of the relaxed structures of the 18 heterostructures, we find that for a given stacking orientation of normal phase TaS_2 on *h*-BN, the most stable CDW structure corresponds to one where atoms in group S1 (+) are nearer N than B, and atoms in group S2 (−) are nearer B than N. The same outcome is also obtained if a normal phase TaS_2 is allowed to relax to the CDW phase naturally, as shown in Structures I and II in Figure 6c,d. This preference is consistent with the negative Bader charge for N and positive Bader charge for B.[40] Specifically, the negatively charged N atoms stabilize group S1 (+) by pushing the negatively charged S atoms away from N and also away from one another (see schematic in Figure 6b). On the other hand, the positively charged B atoms stabilize group S2 (−) by pulling the negatively charged S atoms closer to B and closer to one another. In this way, quite remarkably, the relative positions of B and N atoms, as well as S atoms in the commensurate TaS_2/*h*-BN superlattice, favor the CDW phase in TaS_2 (Figure 6c), which, coincidentally, hosts groups of sulfur atoms, S1 (+) and S2 (−), in exactly the arrangement that is also favored by the positions of B and N atoms in the *h*-BN substrate.

CONCLUSIONS

In summary, we have discovered a room temperature commensurate CDW state on epitaxially grown 2H-TaS_2 on *h*-BN. DFT calculations show that the stabilization of the 3×3 CDW phase can be largely attributed to the interfacial electrostatic interaction between TaS_2 and *h*-BN in the Moiré superlattice of few-layer 3×3 TaS_2 on 4×4 *h*-BN and the absence of charge transfer across the interface. On an epitaxially grown TaS_2/graphene substrate, however, charge transfer interaction suppresses the CDW phase on TaS_2. In addition to charge transfer interactions and interfacial strain that have been used previously for tuning the CDW and superconducting transition temperature, our work suggests that a third control mechanism lies in Moiré-modulated interfacial electrostatic interactions. Additional theoretical and experimental work is needed to fully explore the potential applications engendered by a room temperature commensurate CDW state.

METHODS

The epitaxial growth was carried out in a customized MBE system with a base pressure of $<3 \times 10^{-10}$ Torr. Ultrapure Ta (99.995%, Goodfellow) and sulfur (99.5%, Alfa Aesar) were evaporated from a mini-electron-beam evaporator and a valved sulfur cracker cell, respectively. The temperature of the sulfur crucible cell was set to 383 K. A two-step growth process was applied: in the first stage, the substrate was kept at around 973 K for 3 h to form scattered domains; in the second stage, the substrate temperature was increased to 1073 K and maintained for another 2 h to allow lateral growth and merging of the isolated domains to form a whole film. After growth, both the Ta and sulfur sources were turned off, and the sample was annealed at 1073 K for 30 min before cooling to room temperature at a rate of 10 K/min.

The multilayer *h*-BN was epitaxially grown on a wafer sized c-plane sapphire by a low-pressure CVD method.[41] Ammonia borane (97% purity, Sigma-Aldrich) was used as the B and N sources. After the furnace was increased to 1673 K under a mixed H_2/Ar gas, ammonia borane was heated to 403 K and the growth of *h*-BN maintained for 30 min at a controlled pressure of 0.1 Torr. After that, the furnace was cooled down under a mixed H_2/Ar gas. The basic characterizations of the grown wafer scale *h*-BN/sapphire film are reported in our previous paper.[42]

Atomic force microscopy was performed using Bruker Dimension FastScan atomic force microscope in noncontact mode at room temperature. The Raman spectroscopy measurements were performed by a WITec Alpha300 Series confocal Raman system with 2400 g/mm grating with a 532 nm excitation laser. A combination with a Bragg notch filter allows the measurements of the low-frequency Raman modes down to approximately ~10 cm^{-1}. The beam spot size of the excitation laser is focused around 1 μm by a 50× long working distance (LWD) objective. To avoid laser-induced sample damage, the power of the laser was strictly controlled below 2 mW. An integration time of 180 s was used to obtain the spectra. The temperature dependent Raman measurements were achieved by interfacing the Linkam optical DSC600 and LNP95 cooling system. The TaS_2 samples were introduced into a vacuum chamber with a cryostat. Furthermore, in order to avoid sample degradation caused by the solution-based transfer method, the TaS_2 atomic layers were directly grown by MBE on an *h*-BN (or graphene) flake that was pretransferred onto a Mo-TEM grid. STEM-ADF imaging was carried out on an aberration-corrected JEOL ARM-200F equipped with a cold field emission gun, operating at 80 kV, and an ASCOR probe corrector. The convergence semiangle of the probe was ≈30 mrad. STEM-MAADF images were collected using a half angle range from ≈30 to 110 mrad, while STEM-HAADF images were collected from ≈85 to 280 mrad. XPS characterizations were performed using a SPECS XR-50 X-ray Mg Kα (1253.7 eV) source with a pass energy of

https://dx.doi.org/10.1021/acsnano.0c00303
ACS Nano 2020, 14, 3917−3926

30 eV and a spot size of 5 mm. A PHOIBOS 150 hemispherical energy analyzer (SPECS, GmbH) was used as the energy analyzer. The binding energies of the XPS spectra were calibrated using Au $4f_{7/2}$ peaks. XPS peak fitting was carried out using a mixed Gaussian–Lorentzian function after a Shirley background subtraction.

Density functional theory calculations were performed using the projector augmented wave method[43,44] and a plane-wave basis set as implemented in the Vienna *ab initio* simulation package (VASP).[45] Density functional perturbation theory was employed to vibrational frequencies at the Gamma point (VASP) and phonon dispersion (Quantum Espresso[46]). The kinetic energy cutoff for the plane-wave basis set was set to 700 eV for calculating geometric and vibrational properties. A *k*-mesh of 27 × 27 × 15 was adopted to sample the first Brillouin zone of the unit cell of bulk 2H-TaS_2. The mesh density of the *k* points was kept fixed when calculating the properties for few-layer normal and CDW phase H-TaS_2. In the geometry optimization and vibrational frequency calculations, van der Waals interactions were considered at the vdW-DF level with the optB86b functional,[31,47,48] which has been shown to be accurate in describing the structural properties of layered materials.[49] The shape and volume of each supercell were fully optimized. The energy convergence criteria for the self-consistent cycle was 1×10^{-6} eV. All atoms in the supercell were allowed to relax until the residual force per atom was less than 5×10^{-4} eV·Å^{-1}. Total energies were also computed using the GGA+*U* method to consider a strong on-site Coulomb interaction of *d* localized electrons of Ta.[34] U = 2.5 eV was estimated using a linear-response method.[35] Electronic band structures were calculated using the Perdew–Burke–Ernzerhof (PBE) functional with spin–orbit coupling (SOC). The phonon dispersion shown in Figure S8a was calculated using the PBE-D3 functional.[50]

ASSOCIATED CONTENT

Supporting Information

The Supporting Information is available free of charge at https://pubs.acs.org/doi/10.1021/acsnano.0c00303.

AFM images under different growth stages, basic characterizations of the wafer-scale film, XPS spectra, calculated lattice constants and the Ta–Ta distance in the normal and CDW phases, simulated FFT images, vibrational properties, and effects of the strain on the CDW formation energy (PDF)

AUTHOR INFORMATION

Corresponding Authors

Su Ying Quek – *Centre for Advanced 2D Materials and Department of Physics, National University of Singapore, 117546, Singapore*; Email: phyqsy@nus.edu.sg

Kian Ping Loh – *Department of Chemistry and Centre for Advanced 2D Materials, National University of Singapore, 117543, Singapore*; orcid.org/0000-0002-1491-743X; Email: chmlohkp@nus.edu.sg

Authors

Wei Fu – *Department of Chemistry and Centre for Advanced 2D Materials, National University of Singapore, 117543, Singapore*

Jingsi Qiao – *Centre for Advanced 2D Materials, National University of Singapore, 117546, Singapore*

Xiaoxu Zhao – *Department of Materials Science and Engineering, National University of Singapore, 117575, Singapore*; orcid.org/0000-0001-9746-3770

Yu Chen – *School of Physical & Mathematical Sciences, Nanyang Technological University, 639798, Singapore*

Deyi Fu – *Centre for Advanced 2D Materials, National University of Singapore, 117546, Singapore*; orcid.org/0000-0003-1365-8963

Wei Yu – *Department of Chemistry, National University of Singapore, 117543, Singapore*; orcid.org/0000-0003-3468-3439

Kai Leng – *Department of Chemistry, National University of Singapore, 117543, Singapore*; orcid.org/0000-0003-3408-5033

Peng Song – *Department of Chemistry, National University of Singapore, 117543, Singapore*

Zhi Chen – *Department of Chemistry, National University of Singapore, 117543, Singapore*

Ting Yu – *School of Physical & Mathematical Sciences, Nanyang Technological University, 639798, Singapore*; orcid.org/0000-0001-5782-1588

Stephen J. Pennycook – *Department of Materials Science and Engineering, National University of Singapore, 117575, Singapore*; orcid.org/0000-0002-3210-6323

Complete contact information is available at: https://pubs.acs.org/10.1021/acsnano.0c00303

Author Contributions

#W.F., J.S.Q., and X.X.Z. contributed equally to this work. W.F., X.X.Z., and K.P.L. conceived the idea. S.Y.Q. and K.P.L. supervised the execution of the whole work. W.F. grew the samples. X.X.Z. performed the electron microscopy experiments and data analysis. J.S.Q. and S.Y.Q. did the DFT calculation and data analysis. W.F. and Y.C. measured the Raman data. W.Y. did the XPS measurement. All the authors discussed the results. All authors participated in writing the manuscript.

Notes

The authors declare no competing financial interest.

ACKNOWLEDGMENTS

K.P.L thanks the A*STAR Project "Scalable Growth of Ultrathin Ferroelectric Materials for Memory Technologies, Grant Number A1983c0035" and support from Centre for Advanced 2D Materials, NUS. S.Y.Q. thanks the National Research Foundation Competitive Research Program "Two-Dimensional Covalent Organic Framework: Synthesis and Application (NRF-CRP16-2015-02)" and support from the Singapore National Research Foundation, Prime Minister's Office, under its medium-sized centre program. Computations were performed on the NUS Graphene Research Centre cluster and National Supercomputing Centre Singapore (NSCC). S.J.P. is grateful to the National University of Singapore for funding and MOE for a Tier 2 grant "Atomic scale understanding and optimization of defects in 2D materials" (MOE2017-T2-2-139). T.Y. thanks the MOE for a Tier 2 grant (MOE2018-T2-2-072).

REFERENCES

(1) Grüner, G. The Dynamics of Charge-Dengy Waves. *Rev. Mod. Phys.* **1988**, *60*, 1129–1181.

(2) Manzeli, S.; Ovchinnikov, D.; Pasquier, D.; Yazyev, O. V.; Kis, A. 2D Transition Metal Dichalcogenides. *Nat. Rev. Mater.* **2017**, *2*, 17033.

(3) Xi, X.; Zhao, L.; Wang, Z.; Berger, H.; Forró, L.; Shan, J.; Mak, K. F. Strongly Enhanced Charge-Density-Wave Order in Monolayer $NbSe_2$. *Nat. Nanotechnol.* **2015**, *10*, 765.

(4) Yu, Y.; Yang, F.; Lu, X. F.; Yan, Y. J.; Cho, Y. H.; Ma, L.; Niu, X.; Kim, S.; Son, Y. W.; Feng, D.; Li, S.; Cheong, S. W.; Chen, X. H.; Zhang, Y. Gate-Tunable Phase Transitions in Thin Flakes of 1T-TaS_2. *Nat. Nanotechnol.* **2015**, *10*, 270.

(5) Littlewood, P. B.; Rice, T. M. Theory of the Splitting of Discommensurations in the Charge-Density-Wave State of 2H-$TaSe_2$. *Phys. Rev. Lett.* **1982**, *48*, 27−30.
(6) Zeljkovic, I.; Main, E. J.; Williams, T. L.; Boyer, M. C.; Chatterjee, K.; Wise, W. D.; Yin, Y.; Zech, M.; Pivonka, A.; Kondo, T.; Takeuchi, T.; Ikuta, H.; Wen, J.; Xu, Z.; Gu, G. D.; Hudson, E. W.; Hoffman, J. E. Scanning Tunnelling Microscopy Imaging of Symmetry-Breaking Structural Distortion in the Bismuth-Based Cuprate Superconductors. *Nat. Mater.* **2012**, *11*, 585.
(7) Yusupov, R.; Mertelj, T.; Kabanov, V. V.; Brazovskii, S.; Kusar, P.; Chu, J. H.; Fisher, I. R.; Mihailovic, D. Coherent Dynamics of Macroscopic Electronic Order through a Symmetry Breaking Transition. *Nat. Phys.* **2010**, *6*, 681.
(8) Ishioka, J.; Liu, Y. H.; Shimatake, K.; Kurosawa, T.; Ichimura, K.; Toda, Y.; Oda, M.; Tanda, S. Chiral Charge-Density Waves. *Phys. Rev. Lett.* **2010**, *105*, 176401.
(9) Butz, T.; Ebeling, K. H.; Hagn, E.; Saibene, S.; Zech, E.; Lerf, A. Evidence for the Coexistence of Charge- and Spin-Density Waves in 2H-TaS_2. *Phys. Rev. Lett.* **1986**, *56*, 639−642.
(10) Liu, G.; Debnath, B.; Pope, T. R.; Salguero, T. T.; Lake, R. K.; Balandin, A. A. A Charge-Density-Wave Oscillator Based on an Integrated Tantalum Disulfide−Boron Nitride−Graphene Device Operating at Room Temperature. *Nat. Nanotechnol.* **2016**, *11*, 845.
(11) Zhu, C.; Chen, Y.; Liu, F.; Zheng, S.; Li, X.; Chaturvedi, A.; Zhou, J.; Fu, Q.; He, Y.; Zeng, Q.; Fan, H. J.; Zhang, H.; Liu, W. J.; Yu, T.; Liu, Z. Light-Tunable 1T-TaS_2 Charge-Density-Wave Oscillators. *ACS Nano* **2018**, *12*, 11203−11210.
(12) Wang, Q. H.; Kalantar-Zadeh, K.; Kis, A.; Coleman, J. N.; Strano, M. S. Electronics and Optoelectronics of Two-Dimensional Transition Metal Dichalcogenides. *Nat. Nanotechnol.* **2012**, *7*, 699.
(13) Chhowalla, M.; Shin, H. S.; Eda, G.; Li, L. J.; Loh, K. P.; Zhang, H. The Chemistry of Two-Dimensional Layered Transition Metal Dichalcogenide Nanosheets. *Nat. Chem.* **2013**, *5*, 263.
(14) Wilson, J. A.; Di Salvo, F. J.; Mahajan, S. Charge-Density Waves and Superlattices in the Metallic Layered Transition Metal Dichalcogenides. *Adv. Phys.* **1975**, *24*, 117−201.
(15) Li, L.; Deng, X.; Wang, Z.; Liu, Y.; Abeykoon, M.; Dooryhee, E.; Tomic, A.; Huang, Y.; Warren, J. B.; Bozin, E. S.; Billinge, S. J. L.; Sun, Y.; Zhu, Y.; Kotliar, G.; Petrovic, C. Superconducting Order from Disorder in 2H-$TaSe_{2-x}S_x$. *npj Quantum. npj Quant. Mater.* **2017**, *2*, 11.
(16) Harper, J. M. E.; Geballe, T. H.; DiSalvo, F. J. Thermal Properties of Layered Transition-Metal Dichalcogenides at Charge-Density-Wave Transitions. *Phys. Rev. B* **1977**, *15*, 2943−2951.
(17) Wei, M. J.; Lu, W. J.; Xiao, R. C.; Lv, H. Y.; Tong, P.; Song, W. H.; Sun, Y. P. Manipulating Charge Density Wave Order in Monolayer 1T-$TiSe_2$ by Strain and Charge Doping: A First-Principles Investigation. *Phys. Rev. B: Condens. Matter Mater. Phys.* **2017**, *96*, 165404.
(18) Kansara, S.; Gupta, S. K.; Sonvane, Y. Effect of Strain Engineering on 2D Dichalcogenides Transition Metal: A DFT Study. *Comput. Mater. Sci.* **2018**, *141*, 235−242.
(19) Albertini, O. R.; Liu, A. Y.; Calandra, M. Effect of Electron Doping on Lattice Instabilities in Single-Layer 1H-TaS_2. *Phys. Rev. B: Condens. Matter Mater. Phys.* **2017**, *95*, 235121.
(20) Lian, C. S.; Si, C.; Wu, J.; Duan, W. First-Principles Study of Na-Intercalated Bilayer $NbSe_2$: Suppressed Charge-Density Wave and Strain-Enhanced Superconductivity. *Phys. Rev. B: Condens. Matter Mater. Phys.* **2017**, *96*, 235426.
(21) Calandra, M.; Mazin, I. I.; Mauri, F. Effect of Dimensionality on the Charge-Density Wave in Few-Layer 2H-$NbSe_2$. *Phys. Rev. B: Condens. Matter Mater. Phys.* **2009**, *80*, 241108.
(22) Yang, Y.; Fang, S.; Fatemi, V.; Ruhman, J.; Navarro-Moratalla, E.; Watanabe, K.; Taniguchi, T.; Kaxiras, E.; Jarillo-Herrero, P. Enhanced Superconductivity Upon Weakening of Charge Density Wave Transport in 2H-TaS_2 in the Two-Dimensional Limit. *Phys. Rev. B: Condens. Matter Mater. Phys.* **2018**, *98*, No. 035203.
(23) Luo, Z.; Kim, S.; Kawamoto, N.; Rappe, A. M.; Johnson, A. T. C. Growth Mechanism of Hexagonal-Shape Graphene Flakes with Zigzag Edges. *ACS Nano* **2011**, *5*, 9154−9160.
(24) Liu, L.; Park, J.; Siegel, D. A.; McCarty, K. F.; Clark, K. W.; Deng, W.; Basile, L.; Idrobo, J. C.; Li, A. P.; Gu, G. Heteroepitaxial Growth of Two-Dimensional Hexagonal Boron Nitride Templated by Graphene Edges. *Science* **2014**, *343*, 163−167.
(25) Kobayashi, Y.; Fukui, K. I.; Enoki, T.; Kusakabe, K.; Kaburagi, Y. Observation of Zigzag and Armchair Edges of Graphite Using Scanning Tunneling Microscopy and Spectroscopy. *Phys. Rev. B: Condens. Matter Mater. Phys.* **2005**, *71*, 193406.
(26) Muller, D. A.; Nakagawa, N.; Ohtomo, A.; Grazul, J. L.; Hwang, H. Y. Atomic-Scale Imaging of Nanoengineered Oxygen Vacancy Profiles in $SrTiO_3$. *Nature* **2004**, *430*, 657−661.
(27) Abe, E.; Pennycook, S. J.; Tsai, A. P. Direct Observation of a Local Thermal Vibration Anomaly in a Quasicrystal. *Nature* **2003**, *421*, 347−350.
(28) Lefcochilos-Fogelquist, H. M.; Albertini, O. R.; Liu, A. Y. Substrate-Induced Suppression of Charge Density Wave Phase in Monolayer 1H-TaS_2 on Au(111). *Phys. Rev. B: Condens. Matter Mater. Phys.* **2019**, *99*, 174113.
(29) Lian, C. S.; Si, C.; Duan, W. Unveiling Charge-Density Wave, Superconductivity, and Their Competitive Nature in Two-Dimensional $NbSe_2$. *Nano Lett.* **2018**, *18*, 2924−2929.
(30) Dion, M.; Rydberg, H.; Schroder, E.; Langreth, D. C.; Lundqvist, B. I. van der Waals Density Functional for General Geometries. *Phys. Rev. Lett.* **2004**, *92*, 246401.
(31) Lee, K.; Murray, É. D.; Kong, L.; Lundqvist, B. I.; Langreth, D. C. Higher-Accuracy van der Waals Density Functional. *Phys. Rev. B: Condens. Matter Mater. Phys.* **2010**, *82*, No. 081101.
(32) Zheng, F.; Zhou, Z.; Liu, X.; Feng, J. First-Principles Study of Charge and Magnetic Ordering in Monolayer $NbSe_2$. *Phys. Rev. B: Condens. Matter Mater. Phys.* **2018**, *97*, No. 081101.
(33) Galvis, J. A.; Rodière, P.; Guillamon, I.; Osorio, M. R.; Rodrigo, J. G.; Cario, L.; Navarro-Moratalla, E.; Coronado, E.; Vieira, S.; Suderow, H. Scanning Tunneling Measurements of Layers of Superconducting 2H-$TaSe_2$: Evidence for a Zero-Bias Anomaly in Single Layers. *Phys. Rev. B: Condens. Matter Mater. Phys.* **2013**, *87*, No. 094502.
(34) Cococcioni, M. The LDA+ U Approach: A Simple Hubbard Correction for Correlated Ground States. In *Correlated Electrons: From Models to Materials Modeling and Simulation*; Verlag des Forschungszentrum Jülich: Jülich, Germany, 2012.
(35) Cococcioni, M.; de Gironcoli, S. Linear Response Approach to the Calculation of the Effective Interaction Parameters in the LDA+U Method. *Phys. Rev. B: Condens. Matter Mater. Phys.* **2005**, *71*, No. 035105.
(36) Sugai, S.; Murase, K.; Uchida, S.; Tanaka, S. Studies of Lattice Dynamics in 2H-TaS_2 by Raman Scattering. *Solid State Commun.* **1981**, *40*, 399−401.
(37) Zhang, K.; Cao, Z. Y.; Chen, X. J. Effects of Charge-Density-Wave Phase Transition on Electrical Transport and Raman Spectra in 2H-Tantalum Disulfide. *Appl. Phys. Lett.* **2019**, *114*, 141901.
(38) Wang, Z.; Chu, L.; Li, L.; Yang, M.; Wang, J.; Eda, G.; Loh, K. P. Modulating Charge Density Wave Order in a 1T-TaS_2/Black Phosphorus Heterostructure. *Nano Lett.* **2019**, *19*, 2840−2849.
(39) Gan, L. Y.; Zhang, L. H.; Zhang, Q.; Guo, C. S.; Schwingenschlogl, U.; Zhao, Y. Strain Tuning of the Charge Density Wave in Monolayer and Bilayer 1T-TaS_2. *Phys. Chem. Chem. Phys.* **2016**, *18*, 3080−3085.
(40) Matta, C.; Boyd, R. *The Quantum Theory of Atoms in Molecules: From Solid State to DNA and Drug Design*; Wiley-VCH Verlag: Weinheim, 2007.
(41) Jang, A.; Hong, S.; Hyun, C.; Yoon, S.; Kim, G.; Jeong, H.; Shin, T.; Park, S.; Wong, K.; Kwak, S.; Park, N.; Yu, K.; Choi, E.; Mishchenko, A.; Withers, F.; Novoselov, K.; Lim, H.; Shin, H. Wafer-Scale and Wrinkle-Free Epitaxial Growth of Single-Orientated Multilayer Hexagonal Boron Nitride on Sapphire. *Nano Lett.* **2016**, *16*, 3360−3366.

https://dx.doi.org/10.1021/acsnano.0c00303
ACS Nano 2020, 14, 3917−3926

(42) Fu, D.; Zhao, X.; Zhang, Y.; Li, L.; Xu, H.; Jang, A.; Yoon, S.; Song, P.; Poh, S.; Ren, T.; Ding, Z.; Fu, W.; Shin, T.; Shin, H.; Pantelides, S.; Zhou, W.; Loh, K. Molecular Beam Epitaxy of Highly Crystalline Monolayer Molybdenum Disulfide on Hexagonal Boron Nitride. *J. Am. Chem. Soc.* **2017**, *139*, 9392−9400.
(43) Blochl, P. E. Projector Augmented-Wave Method. *Phys. Rev. B: Condens. Matter Mater. Phys.* **1994**, *50*, 17953−17979.
(44) Kresse, G.; Joubert, D. From Ultrasoft Pseudopotentials to the Projector Augmented-Wave Method. *Phys. Rev. B: Condens. Matter Mater. Phys.* **1999**, *59*, 1758−1775.
(45) Kresse, G.; Furthmüller, J. Efficient Iterative Schemes for *Ab Initio* Total-Energy Calculations Using a Plane-Wave Basis Set. *Phys. Rev. B: Condens. Matter Mater. Phys.* **1996**, *54*, 11169−11186.
(46) Giannozzi, P.; Baroni, S.; Bonini, N.; Calandra, M.; Car, R.; Cavazzoni, C.; Ceresoli, D.; Chiarotti, G. L.; Cococcioni, M.; Dabo, I.; Dal Corso, A.; de Gironcoli, S.; Fabris, S.; Fratesi, G.; Gebauer, R.; Gerstmann, U.; Gougoussis, C.; Kokalj, A.; Lazzeri, M.; Martin-Samos, L.; et al. QUANTUM ESPRESSO: A Modular and Open-Source Software Project for Quantum Simulations of Materials. *J. Phys.: Condens. Matter* **2009**, *21*, 395502.
(47) Klimes, J.; Bowler, D. R.; Michaelides, A. Chemical Accuracy for the van der Waals Density Functional. *J. Phys.: Condens. Matter* **2010**, *22*, No. 022201.
(48) Klimes, J.; Bowler, D. R.; Michaelides, A. van der Waals Density Functionals Applied to Solids. *Phys. Rev. B: Condens. Matter Mater. Phys.* **2011**, *83*, 195131.
(49) Qiao, J.; Kong, X.; Hu, Z. X.; Yang, F.; Ji, W. High-Mobility Transport Anisotropy and Linear Dichroism in Few-Layer Black Phosphorus. *Nat. Commun.* **2014**, *5*, 4475.
(50) Grimme, S.; Antony, J.; Ehrlich, S.; Krieg, H. A Consistent and Accurate *Ab Initio* Parametrization of Density Functional Ddispersion Correction (DFT-D) for the 94 Elements H-Pu. *J. Chem. Phys.* **2010**, *132*, 154104.

https://dx.doi.org/10.1021/acsnano.0c00303
ACS Nano 2020, 14, 3917−3926